Binding of He n V clusters to -Fe grain boundaries

M. A. Tschopp, F. Gao, and K. N. Solanki

Articles you may be interested in

Binding energetics of substitutional and interstitial helium and di-helium defects with grain boundary structure in -Fe
J. Appl. Phys. **115**, 033503 (2014); 10.1063/1.4861719

Theoretical study of AlnV+ clusters and their interaction with Ar
J. Chem. Phys. **139**, 214305 (2013); 10.1063/1.4834595

An intramolecular vibrationally excited intermolecular potential for He–OCS: Globally tested by simulation of vibrational shifts for OCS in He N N = 1 100 Clusters
J. Chem. Phys. **137**, 234310 (2012); 10.1063/1.4772186

Theoretical characterization of intermolecular vibrational states through the multi-configuration time dependent Hartree approach: The He2,3ICl clusters
J. Chem. Phys. **135**, 244309 (2011); 10.1063/1.3671611

Identification of boron clusters in silicon crystal by B1s core-level X-ray photoelectron spectroscopy: A first-principles study
Appl. Phys. Lett. **99**, 191901 (2011); 10.1063/1.3658030

Binding of He$_n$V clusters to α-Fe grain boundaries

M. A. Tschopp,[1,a)] F. Gao,[2] and K. N. Solanki[3]

[1]*U.S. Army Research Laboratory, Aberdeen Proving Ground, Maryland 21005, USA*
[2]*Pacific Northwest National Laboratory, Richland, Washington 99352, USA*
[3]*Arizona State University, Tempe, Arizona 85287, USA*

The objective of this research is to explore the formation/binding energetics and length scales associated with the interaction between He$_n$V clusters and grain boundaries in bcc α-Fe. In this work, we calculated formation/binding energies for 1–8 He atoms in a monovacancy at all potential grain boundary (GB) sites within 15 Å of the ten grain boundaries selected (122106 simulations total). The present results provide detailed information about the interaction energies and length scales of 1–8 He atoms with grain boundaries for the structures examined. A number of interesting new findings emerge from the present study. First, the $\Sigma 3(112)$ "twin" GB has significantly lower binding energies for all He$_n$V clusters than all other boundaries in this study. For all grain boundary sites, the effect of the local environment surrounding each site on the He$_n$V formation and binding energies decreases with an increasing number of He atoms in the He$_n$V cluster. Based on the calculated dataset, we formulated a model to capture the evolution of the formation and binding energy of He$_n$V clusters as a function of distance from the GB center, utilizing only constants related to the maximum binding energy and the length scale. © *2014 AIP Publishing LLC.*
[http://dx.doi.org/10.1063/1.4883357]

I. INTRODUCTION

The ability to predict the mechanical behavior of current and future nuclear power reactors necessitates understanding the atomic interactions associated both with radiation damage phenomena and grain boundaries in polycrystalline nuclear materials.[1] In particular, future fusion reactors will produce a much larger amount of both He and H as compared to fission reactors, hence the microstructure of the structural materials used in fusion reactors will be much more sensitive to interactions with He defects.[2,3] In terms of radiation damage, the production of helium through (n, α) transmutation reactions causes both microstructure evolution and drastic property changes in the first-wall and blanket structural materials of fusion reactors. The production of single helium atoms and small He clusters in the metal lattice is inherently a problem that occurs at the nanoscale. The subsequent diffusion of He and He clusters results in the nucleation and growth of He bubbles on grain boundaries and within the lattice, which lead to a macroscopic deterioration of material properties including void swelling, surface roughening and blistering, and high temperature intergranular embrittlement [e.g., Refs. 1–9]. While the production and diffusion of He occurs at the nanoscale, these other processes develop at larger length scales over long time scales, which necessitates developing predictive multiscale models for material behavior under irradiation conditions that couples multiple simulation methods at different length and time scales. Developing this predictive capability will require an understanding of the mechanisms associated with radiation damage phenomena, of the He interaction with microstructures and of the associated uncertainties.

It is well known that He interactions in Fe play an important role in the mechanical behavior of steel alloys. There have been a number of quantum mechanics and molecular dynamics simulations that have examined how He and He clusters affect single crystal lattice properties and physical properties in α-Fe.[10–28] For instance, density functional theory (DFT) simulations have been used to show that interstitial He atoms strongly interact with vacancies and can also be trapped by interstitial atoms (binding energy of 0.3 eV).[10] Ventelon, Wirth, and Domain[24] probed the interactions between He and self-interstitial atoms (SIAs) in α-Fe and found strong binding behavior between interstitial He and SIA clusters, which corresponded with the SIA defect strain field. Other atomistic studies have examined how He and H interact within the single crystal lattice to form complex He–H clusters[27] or how He impacts the production of irradiation-induced point defects in an Fe–Cr matrix.[28] Stewart *et al.*[25,26] recently used several Fe–He potentials[29–31] to show the effect of the interatomic potential on the resulting dynamics of He transport and He clustering in Fe. Ascertaining the reactions that occur and quantifying their energetics are important for a fundamental understanding of how point defects, impurities, substitutional atoms, and helium atoms interact in the single crystal lattice of α-Fe. Furthermore, this information is useful for models that explore the kinetics of He diffusion, trapping (clustering), and detrapping (emission), such as rate theory models,[32–35] kinetic Monte Carlo models,[36,37] and/or phase field models.[38,39]

The grain boundary itself and its atomic configuration within these alloy systems plays a significant role in trapping

---

point defects and various atomic species. There have been a number of recent studies using both first principles and molecular dynamic simulations that have examined how solutes and impurities segregate to grain boundaries within bcc metals.[40–47] Despite this fact, there have been relatively few studies that have focused on He interactions with grain boundaries.[48–58] These prior works have been significant for understanding the migration paths and mechanisms of He for a few boundaries using the dimer method,[49,51] understanding migration of interstitial He in different grain boundaries using molecular dynamics,[52] understanding how the grain boundary strength is affected by He[53,54] or He bubbles,[55] or understanding the diffusion and stability of He defects in grain boundaries using first principles.[56,57] For instance, Kurtz and Heinisch[48] used a Finnis–Sinclair potential (detailed in Morishita *et al.*[14]) to show that interstitial He was more strongly bound to the grain boundary core than substitutional He. Kurtz and Heinisch also found that the maximum He binding energy increases linearly with the grain boundary excess free volume, similar to prior work in fcc nickel.[59] In subsequent studies, Gao, Heinisch, and Kurtz[49] found a relationship between the maximum binding energy and grain boundary energy as well. Additionally, Gao *et al.* started to detail the diffusion trajectories of interstitial and substitutional He atoms along a $\Sigma 3$ and $\Sigma 11$ grain boundary and found that the dimensionality of migration of interstitial He may depend on temperature (e.g., in the $\Sigma 3(112)$ boundary). Some recent work has utilized first principles to quantify binding strengths of He and He-vacancy clusters at the $\Sigma 5(310)$ symmetric tilt grain boundary (STGB).[57] There are still a number of unresolved issues relating to how He interacts with grain boundaries, though. For instance, these studies often focus on one He atom in interstitial or substitutional sites, but often do not extend to multiple He atoms interacting with grain boundary sites. Also, atomistic studies often have not examined a wide range of grain boundary structures to understand the influence of macroscopic variables on He interactions. Moreover, while the highly non-uniform He binding energies in the grain boundary core have been previously pointed out,[48] relating these to per-atom metrics based on the grain boundary local environment has not been pursued as frequently. Additionally, while there is an increasing awareness of interatomic potential effects, many of the interatomic potentials used previously for some of these grain boundary studies have been improved upon with updated interatomic potential formulations[15,30,60] and/or more recent quantum mechanics results showing how magnetism affects He defects in α-Fe.[12,23,61]

It has been well established that the presence of He and vacancies at the grain boundary leads to the formation/nucleation of He bubbles, both computationally and experimentally. Single helium atoms created initially are very mobile and can be easily trapped by microstructure features (e.g., grain boundaries and dislocations) forming small He clusters or He–V clusters. Furthermore, it has been shown that the mobility of He atoms trapped in a monovacancy decreases significantly and diffusion can only occur by an often energetically unfavorable dissociation mechanism. Hence, these

small clusters inevitably result in the growth of large helium bubbles in GBs, as has been observed in experiments. Thus, it is important to gain the basic knowledge of their binding properties to GBs and their migration behavior within GBs. Since He-vacancy clusters and interactions are a complex issue, the present study provides initial results for future more comparative studies at higher scales, which may allow for a quantitative understanding of experimental results. In this study, it is expected that a general trend of the binding properties of He–V clusters can be established, which can be used in mesoscale simulation of He bubble nucleation and growth.

Therefore, in the present work, we have focused on how the local grain boundary structure interacts with He atoms and how the local atomic environment at the boundary influences the binding energetics of He_nV clusters with up to 8 He atoms inside a monovacancy. Recently, Tschopp and colleagues utilized an iterative approach to systematically quantify the interactions between point defects, carbon, hydrogen, and helium with Fe grain boundaries.[46,47,58,62,63] Herein, this approach is applied along with using multiple different starting positions, or instantiations, about each site to more precisely probe the formation and binding energy landscape about ten grain boundaries. In this paper, we present this approach for eight He_nV clusters and we explore how the grain boundary structure interacts with He_nV clusters using molecular static calculations. Moreover, we have also explored how different per-atom local environment metrics compare with the calculated energies for the different He_nV clusters and the energetics of incorporating additional interstitial He atoms into the He_nV clusters. A number of interesting new findings emerge from the present study. First, the $\Sigma 3(112)$ "twin" GB has significantly lower binding energies for all He_nV clusters than all other boundaries in this study. For all grain boundary sites, the effect of the local environment surrounding each site on the He_nV formation and binding energies decreases with an increasing number of He atoms in the He_nV cluster. Based on the calculated dataset, we formulated a model to capture the evolution of the formation and binding energy of He_nV clusters as a function of distance from the GB center, utilizing only constants related to the maximum binding energy and the length scale. This work significantly enhances our understanding of the energetics involved with how the grain boundary structure interacts with He_nV clusters and how ultimately this may affect He (re-)combination and embrittlement near grain boundaries in polycrystalline steels.

II. METHODOLOGY

A. Grain boundaries

The interaction between helium–vacancy clusters and iron grain boundaries was investigated by using ten different grain boundaries and multiple different He_nV clusters ($n = 1$–8) for multiple sites (866 total sites) within 15 Å of the boundary (122106 simulations total). Table I lists the ten grain boundaries studied, their dimensions in terms of lattice units, the number of atoms and the interfacial energy. These grain boundaries represent the ten low coincident site lattice

TABLE I. Dimensions of the bicrystalline simulation cells used in this work along with the Σ value of the boundary, the grain boundary plane (normal to the y-direction), the misorientation angle θ about the corresponding tilt axis (z-direction), the grain boundary energy, and the number of atoms. The cell dimensions were chosen to ensure convergence of the formation and binding energies of the inserted He_nV clusters.

Sigma and GB plane	GB tilt direction	θ (°)	GB energy (mJ m^{-2})	x (Å)	y (nm)	z (Å)	Number of atoms	Free volume (Å^3/Å^2)
$\Sigma3(111)$	$\langle110\rangle$	109.47	1308	21.0	24.8	16.2	7200	0.35
$\Sigma3(112)$	$\langle110\rangle$	70.53	260	14.8	25.2	16.2	5184	0.01
$\Sigma5(210)$	$\langle100\rangle$	53.13	1113	19.2	24.5	14.3	5730	0.35
$\Sigma5(310)$	$\langle100\rangle$	36.87	1008	18.1	25.3	14.3	5600	0.30
$\Sigma9(221)$	$\langle110\rangle$	141.06	1172	17.1	24.2	16.2	5728	0.19
$\Sigma9(114)$	$\langle110\rangle$	38.94	1286	24.2	25.5	16.2	8576	0.35
$\Sigma11(113)$	$\langle110\rangle$	50.48	1113	26.8	24.7	16.2	9152	0.26
$\Sigma11(332)$	$\langle110\rangle$	129.52	1020	18.9	24.1	16.2	6336	0.21
$\Sigma13(510)$	$\langle100\rangle$	22.62	1005	14.6	26.1	14.3	4660	0.27
$\Sigma13(320)$	$\langle100\rangle$	67.38	1108	20.6	24.7	14.3	6220	0.23

(CSL) boundaries ($\Sigma \leq 13$) within the $\langle100\rangle$ and $\langle110\rangle$ STGB systems. This is a subset of those boundaries used in prior studies of point defect absorption (vacancies and self-interstitial atoms) by a large range of grain boundary structures in pure α-Fe[62,63] and is identical to those used in our previous study of 1–2 atom He defect interactions with grain boundaries.[58]

The current set of boundaries includes four $\langle100\rangle$ STGBs ($\Sigma5$, $\Sigma13$) and six $\langle110\rangle$ STGBs ($\Sigma3$, $\Sigma9$, $\Sigma11$). Recent experimental characterization of steels has shown that several of these symmetric tilt grain boundaries are observed at a concentration higher than random grain boundaries.[64,65] For example, Beladi and Rollett quantified that the $\Sigma3(112)$ symmetric tilt grain boundary is observed at >10 multiples of a random distribution (MRD) of grain boundaries,[64,65] i.e., much larger than would be expected. While the experimental observation of $\langle100\rangle$ symmetric tilt grain boundaries ($\Sigma5$, $\Sigma13$ GBs) is below 1 MRD, these grain boundaries are commonly used in DFT studies due to the low periodic distances required in the grain boundary plane. The present set of boundaries is smaller than those previously explored[62,63] for two reasons. First, since we explored multiple starting configurations for the He_nV clusters in this study, a larger number of simulations were required for each grain boundary than for the point defect studies, which only considered a single vacancy or self-interstitial atom. Second, our prior study[63] found that aside from a few boundaries (e.g., the $\Sigma3(112)$ STGB, included herein), most grain boundaries had similar characteristics with respect to point defect interactions. These results suggest that the ten boundaries explored within can supply ample information about the interaction of He defects with low-Σ grain boundaries, and perhaps shed insight on general high angle grain boundaries as well.

The simulation cell consisted of a 3D periodic bicrystalline structure with two periodic grain boundaries, similar to prior grain boundary studies.[66–68] The two mirror-image grain boundaries are separated by a minimum distance of 12 nm to eliminate any effects on energies due to the presence of the second boundary. While the grain boundaries were generated using the minimum periodic length in the grain boundary period direction and the grain boundary tilt direction (x- and z- directions, respectively), it was found

that the formation energies for the defects were influenced for periodic lengths below $4a_0$. That is, the periodic image of the defect and/or its influence on the surrounding lattice can significantly affect the defect's formation energy. Hence, multiple replications in the grain boundary tilt direction and the grain boundary period direction were used. For instance, the final dimensions for the $\Sigma5(210)$ GB resulted in a vacancy formation energy far away from the boundary that was within 0.015% of that within a 2000-atom bcc single crystal (i.e., 10 a_0 per side). This criteria resulted in simulation cell sizes on the order of 4660–9152 atoms ($\Sigma13(510)$ and $\Sigma11(113)$, respectively). All of the simulations were performed with a modified version of the MOLDY code.[69–71]

Table I also lists several properties of the ten grain boundaries. First, notice that the grain boundary energies range from 260 to 1308 mJ m^{-2}, although the majority of the CSL boundaries have energies >1000 mJ m^{-2}. Also, all boundaries are high angle grain boundaries, based on a 15° Brandon criterion for low/high angle grain boundaries. Additionally, note that while the misorientation angles θ refer to the conventional misorientation angle-energy relationships (e.g., in Ref. 63), the disorientation angle, or minimum angle to rotate lattice A to lattice B, is the same for the two instances of each Σ boundary. The misorientation angles are based on deviation from the (100) planes in the $\langle100\rangle$ and $\langle110\rangle$ STGB systems. The grain boundary energies are similar to those previously calculated (e.g., $\Sigma5(310)$ and $\Sigma13(320)$ GBs are within 2% and 7%, respectively, of a prior study[72]). The grain boundary structures vary for the ten grain boundaries. Further details on the grain boundary structure are given in Tschopp et al.[63] The grain boundary structures have been compared with computed structures using quantum mechanics, when possible. For instance, Bhattacharya et al. used DFT to calculate grain boundary structures for $\Sigma3(111)$ and $\Sigma11(332)$ GBs,[73] which are identical to those computed in the present work. Moreover, the relationship between the grain boundary energies and excess free volume for the $\Sigma3(111)$ and $\Sigma11(332)$ GBs also agrees with previous studies,[48,73,74] as well as with other studies that have found that the $\Sigma3(112)$ GB has a much lower grain boundary energy and excess free volume in comparison to the $\Sigma3(111)$ GB.[63,74] Additionally, the $\Sigma5(310)$ and $\Sigma9(114)$ GB structures also agree with previously calculated first principles

TABLE II. Previously calculated formation energies for the Fe–He empirical potential (EP)[15] used in the present work compared to other empirical potentials[30,79] and DFT (VASP and SIESTA) results.[11,12,23,30,61]

Cluster	HeV (eV)	He_{oct} (eV)	He_{tet} (eV)	He_2V (eV)	He_2 (eV)
VASP[30]	4.08 (3.73)[a]	4.60	4.37	6.63	8.72
VASP[23]	4.34	4.75	4.40	…	…
SIESTA[11]	4.22	4.58	4.39	…	…
EP[79]	3.87	4.57	4.45	…	…
EP[30]	3.75	4.57	4.26	6.46	9.37
EP[15]	3.76[b]	4.47	4.38	6.87	8.49

[a]The data in parentheses were adjusted by Seletskaia et al.[30] for their empirical potential fitting.

[b]The calculated He formation energies are in agreement with previous results.[15]

structures.[56,57] Also included in this table is the excess free volume, which was calculated using a previous methodology for calculating excess volume[75,76] whereby the volume occupied by the bicrystal simulation cell is compared to an equivalent volume of a perfect single crystal lattice and divided by the total grain boundary area.

B. Interatomic potential

The Fe–He interatomic potential fitted by Gao et al.[15] to *ab initio* calculations using an s-band model was used in the present atomistic modeling. This interatomic potential is based on the electronic hybridization between Fe d-electrons and He s-electrons to describe the Fe–He interaction. The single element potentials utilized in the formulation of this potential are the Ackland and Mendelev (AM) potential for the Fe–Fe interactions[77] and the Aziz et al. Hartree–Fock-dispersion pair potential (Aziz-potential)[78] for the He–He interactions. The atomic configurations and formation energies of both single He defects (substitutional, tetrahedral, and octahedral He) and small interstitial He clusters (He_2V, He_3V, and He–He di-interstitial) were utilized in the fitting process. Calculations using this interatomic potential show that both tetrahedral and octahedral interstitials are stable, with tetrahedral He being the most stable interstitial configuration,[15] which agrees with previous *ab initio* calculations.[23,61] The binding properties of the He_xV and He_x interstitial clusters are in reasonable agreement with *ab initio* and previous potential results. This potential has been previously used to investigate the emission of self-interstitial atoms from small He clusters in the α-Fe matrix and to show the dissociation of a di-interstitial He cluster at temperatures

>400 K. The aforementioned potential is deemed appropriate for studying the He interaction with grain boundaries in this work. In addition, the recent first principles calculations of energetic landscape and diffusion of He in α-Fe grain boundaries demonstrate that the potentials used in the present study satisfactorily describe the He behavior at the GBs.[56] In fact, this study has shown that there is good agreement between the vacancy formation energies for n vacancies ($n \leq 4$) in the Σ3(111) GB between DFT results and the present empirical potential (EP).[56] Furthermore, the present interatomic potential has shown good agreement with DFT results for interstitial and substitutional formation energies for multiple layers and multiple boundaries (Table II).[56]

Previous calculations for He defects with 1–2 atoms[58] have also been compared to recent DFT formation/binding energies for the Σ5(310) GB.[53,57] For instance, Table III compares the minimum formation energy, mean binding energy, and maximum binding energy calculated herein with those from Zhang et al.[53,57] The trend of the data with respect to the ordering of formation energies for different He defects agrees well between the Fe–He interatomic potential and DFT. The minimum formation energies for the Σ5(310) GB are within 12.5% of each other, with a larger discrepancy in the binding energies. The largest E_b^{max} deviation is for the He_1V cluster (−43%), with the other He defects falling within 30% of DFT values. The difference does not appear random; formation energies are consistently higher for the Fe–He potential and binding energies are consistently lower. Hence, the present Fe–He interatomic potential[15] qualitatively agrees with previous DFT calculations[53,57] and both formation/binding energies agree with DFT within the calculated differences.

C. Helium clusters

There are eight different He clusters explored in the present study. These eight He_nV clusters correspond to 1–8 He atoms in a monovacancy, which are denoted as He_1V, He_2V, He_3V, …, He_8V. These He_nV clusters result from removing an Fe atom and placing either a single He atom or multiple He atoms nearby the now-vacant site. For a single He atom in a monovacancy (He_1V), the He atom was simply added in the exact location of the removed Fe atom.

For multiple atoms, a slightly different methodology was used. In the case of He_2V, the two atoms were placed in opposite directions along a randomly oriented vector emanating from the vacant site with equal distances to the vacant site and a total distance >1 Å. Since a single instance may

TABLE III. Comparison of Fe–He interatomic potential[15] and DFT[53,57] formation energies and binding energies (same defect, binding between bulk lattice and GB sites) of various He defects in the Σ5(310) GB.

He atoms	Model	Substitutional He (He_1V)			Interstitial He		
		E_f^{min} (eV)	E_b (eV)	E_b^{max} (eV)	E_f^{min} (eV)	E_b (eV)	E_b^{max} (eV)
1	MD[15]	3.08	$E_b^{mean} = 0.33$	0.68	3.17	$E_b^{mean} = 0.68$	1.21
	DFT[53]	2.93	{0.64, 1.20, 0.58, 0.28}	1.20	2.98	{1.29, 0.71, 1.43}	1.43
2	MD[15]	5.52	$E_b^{mean} = 0.88$	1.35	6.32	$E_b^{mean} = 1.24$	2.17
	DFT[57]	5.08	{1.88, 1.45}	1.88	5.62	{2.78}	2.78

TABLE IV. Bulk formation energies, $E_f^{He_nV,bulk}$, standard deviation of formation energies, std($E_f^{He_nV,bulk}$), and the binding energies of an additional interstitial He atom to various He_nV clusters, $E_b^{He \rightsquigarrow He_nV^x}$ (all in eV).

Cluster	He_1V	He_2V	He_3V	He_4V	He_5V	He_6V	He_7V	He_8V
$E_f^{He_nV,bulk}$	3.707	6.793	9.885	12.856	16.024	18.946	22.012	25.144
std$\left(E_f^{He_nV,bulk}\right)$	…	±0.0001	±0.012	±0.015	±0.020	±0.064	±0.105	±0.092
$E_b^{He \rightsquigarrow He_nV,bulk}$	1.294	1.288	1.409	1.212	1.458	1.314	1.248	…

not obtain the minimum energy dumbbell, twenty different instances of the starting configurations were used for each potential site for the He_2V clusters. For higher numbers of He atoms, multiple locations were randomly chosen for the He atoms, given the constraint that any two He atoms could not be closer than 1 Å. Again, 20 different starting positions were used. This number of instances (20) was sufficient to obtain a near constant mean formation energy for interstitial He atom (maximum deviation of 0.4% of bulk value, mean deviation of 0.03% of bulk value) in the bulk region far away from the grain boundary.[58] To examine whether 20 different starting instantiations is sufficient to locate a minimum energy He_nV cluster, we used the previously described methodology to create 100 different minimized He_nV clusters for $n = 1–8$ in a 2000-atom bcc single crystal lattice. The formation energies and their standard deviations are presented in Table IV. First, the standard deviation of the formation (and binding) energies is small; even if the obtained minimum energy He_nV clusters are different, the energy difference is minor. Second, based on randomly drawing 20 energies from these distributions 1 000 000 times, the minimum formation energy of the 20 samples are within 0.25% of the minimum formation from the 100 samples 100% of the time, i.e., 20 samples should give a reasonable approximation of the "global" minimum energy He_nV cluster configuration.

Figure 1 shows the minimum energy He_nV clusters surrounding the central atom site in the bcc unit cell, where the blue atoms represent the initial position of Fe atoms in the bcc unit cell to indicate the scale of the He_nV cluster dimensions. First, despite the randomly oriented starting configuration, the He_2V cluster forms the He_2 dumbbell in the $\langle 100 \rangle$ direction in all 100 cases with a formation energy of 6.7934 eV ± 1.4243 × 10^{-4} eV and a distance of 1.6304 Å ± 8.8 × 10^{-5} Å. These results are in agreement with DFT results and provide confidence that the minimization technique is able to obtain the minimum energy configurations. The subsequent He_nV cluster configurations minimize to a number of different configurations, whereby the number of configurations increases with the number of He atoms in the monovacancy. Interestingly, the He_nV cluster configurations are characterized by a balance of (i) He atoms trying to be close to low energy tetrahedral and/or octahedral sites and (ii) maintain an optimal distance from each other and symmetry, if possible. For instance, the He_3V cluster is similar to the He_2V cluster, whereby two He atoms are very similar to the He_2 $\langle 100 \rangle$ dumbbell with a third He atom close to a low energy octahedral site. The minimum energy configuration for the He_6V cluster is highly symmetric with all 6 He atoms located near the octahedral sites. Again, also interesting is that the He_7V cluster has two central He atoms in a He_2 $\langle 100 \rangle$ dumbbell with five He atoms in a pentagonal configuration (fivefold symmetry) whereby the five atoms are near to low energy tetrahedral (e.g., top two He atoms) and octahedral (e.g., bottom He atom) sites. While the exact geometry of the He clusters at the grain boundary is not explored in the present study, in part due to the complexity of the local neighborhoods, the single crystal configurations suggest that the individual He atoms of the He_nV clusters will be located near low energy interstitial sites within the grain boundary region.
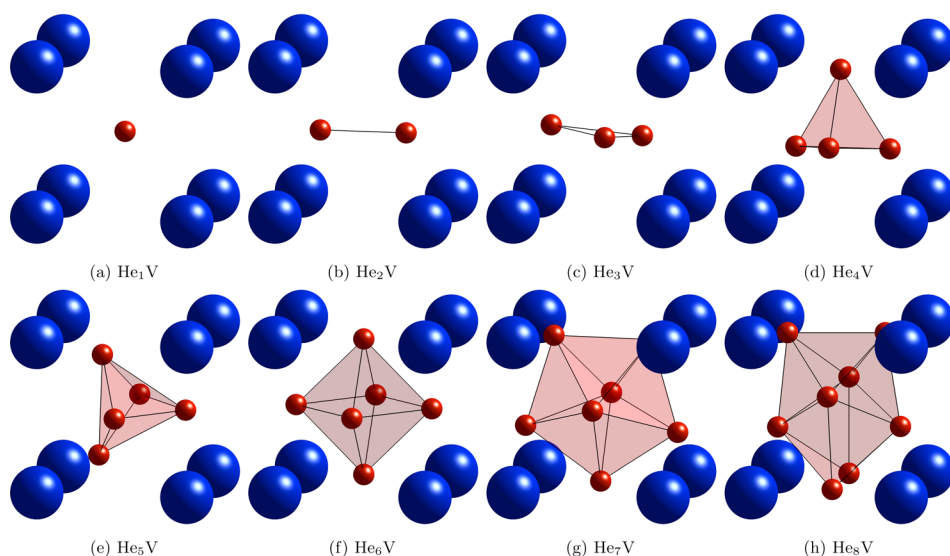

(a) He_1V (b) He_2V (c) He_3V (d) He_4V

(e) He_5V (f) He_6V (g) He_7V (h) He_8V

FIG. 1. The minimum energy (from 100 different instantiations) He_nV cluster configurations for $n = 1–8$ He (red atoms) in a 2000-atom bcc Fe simulation cell (blue atoms shown in undeformed lattice positions to indicate scale). The shaded polygon for $n \geq 4$ indicates the convex hull of the configurations.

D. Formation and binding energies

The formation energies for the He_nV clusters can then be calculated as a function of spatial location of sites and their proximity to the grain boundary. The formation energy for a He_nV cluster containing n He atoms in a monovacancy at site α of a grain boundary configuration is given by

$$E_f^{He_nV^\alpha} = \left(E_{tot}^{He_nV^\alpha} + E_c^{Fe}\right) - \left(E_{tot}^{GB}\right). \qquad (1)$$

Here, $E_{tot}^{He_nV^\alpha}$ is the total energy of the grain boundary configuration with the He_nV cluster at site α, E_{tot}^{GB} is the total energy of the grain boundary without any defects, and E_c^{Fe} is the cohesive energy of bcc Fe ($E_c^{Fe} = 4.013\,\text{eV}$). The cohesive energy of He is negligible and not included in Eq. (1). The formation energies of various He_nV clusters in the bulk, calculated from atom sites far from the boundary, are given in Table IV.

The binding energy of He atoms and He_nV clusters to each other and to the grain boundary is also of interest. The binding energy uses the formation energies to compute whether there is an energetic advantage to two defects being in near proximity to one another or an energetic penalty based on their proximity. In the following paragraphs, two different binding energies are presented: (1) He binding to a He_nV cluster at site α, $E_b^{He^\alpha \rightsquigarrow He_nV^\alpha}$ (Eq. (2)), and (2) a He_nV cluster binding to the grain boundary at site α, $E_b^{He_nV^\alpha}$ (Eq. (3)). The binding energy of an additional He atom to a He_nV cluster is presented in the single crystal only (Table IV), while the remainder of this work focuses on the binding energy between the He_nV cluster and the grain boundary.

First, the binding energy of a He_nV with an additional interstitial He atom is of interest. For instance, in this scenario, we would like to know if a He atom in an interstitial location is either attracted to or repelled from the He_nV cluster. An interstitial He atom is chosen instead of a low energy substitutional He atom, because substitutional He atom can be considered as a trapped He interstitial in a vacancy whereas, in contrast, interstitial He atoms are highly mobile and more likely to bind with He_nV clusters. This binding energy is given by

$$E_b^{He^\alpha \rightsquigarrow He_nV^\alpha} = \left(E_f^{He_nV^\alpha} + E_f^{He^\alpha}\right) - E_f^{He_{n+1}V^\alpha}, \qquad (2)$$

where $E_f^{He^\alpha}$ is the formation energy of an interstitial He atom at site α in the absence of the He_nV cluster. For the purposes of this work, the bulk formation energy of interstitial He is used ($E_f^{He^\alpha} = 4.38\,\text{eV}$) to show the relative binding energy to a He_nV cluster in the *single crystal* lattice as a function of n. Future work will explore how Eq. (2) changes as a function of position near the grain boundary (i.e., changing site α); this calculation is more complex as it involves the binding energy of interstitial He and He_nV to the grain boundary as well as with each other. Table IV lists the binding energy of attracting an additional He to the He_nV cluster in the bulk, e.g., an interstitial He binding to a He_2V cluster to produce a He_3V cluster will decrease the system energy by 1.288 eV. Adding an interstitial He atom to a monovacancy to make

He_1V is slightly different from Eq. (2), but uses the formation energy of a vacancy ($E_f^v = 1.72\,\text{eV}$ in bulk) at site α instead. It is noted that using substitutional He as a reference state for Eq. (2) instead of interstitial He will only shift the values; the general trend will be the same. Interestingly, while $E_b^{He^\alpha \rightsquigarrow He_nV^\alpha}$ generally falls within the range of 1.2–1.5 eV for $n = 1$–8, there are slightly higher $E_b^{He^\alpha \rightsquigarrow He_nV^\alpha}$ values for He_3V and He_5V; that is, there is an even stronger binding energy for an interstitial to form He_4V and He_6V (perhaps due to symmetry, e.g., see He_6V in Fig. 1).

Second, the binding energy of a He_nV cluster with the grain boundary is of interest and is the primary focus of this work. The total binding energy of a He_nV cluster interacting with the GB can be directly calculated from the formation energies of the He_nV cluster in the bulk and the He_nV cluster at the GB. For instance, the binding energy for a He_nV cluster at site α is given by

$$E_b^{He_nV^\alpha} = E_f^{He_nV, bulk} - E_f^{He_nV^\alpha}, \qquad (3)$$

where $E_f^{He_nV, bulk}$ and $E_f^{He_nV^\alpha}$ are the formation energies of a He_nV cluster either in the bulk or at site α, respectively. It can be seen that a positive binding energy represents that it is energetically favorable for the He_nV cluster to segregate to the GB, while a negative binding energy represents that the He_nV cluster does not want to segregate to the GB. In this work, for He_nV clusters ($n \geq 2$), the formation energy used for a particular He_nV cluster at site α is the "minimum" formation energy from the twenty different instantiations (and the binding energy is maximum at site α), i.e.,

$$\bar{E}_f^{He_nV^\alpha} = \min\left(E_f^{He_nV^\alpha}\right), \quad \bar{E}_b^{He_nV^\alpha} = \max\left(E_b^{He_nV^\alpha}\right). \qquad (4)$$

Previous work explored the extreme values (minimum E_f or maximum E_b), mean, and standard deviation of the formation/binding energies from 20 instantiations of He atoms/clusters and utilized the mean formation energy to better capture the stochastic variation of these values as a function of spatial position. However, as the number of He atoms in the He_nV cluster increases, the number of different possible minimum energy configurations also increases, some of which have much higher energies than the most energetically stable He_nV cluster. Therefore, the remainder of the analysis will focus on the minimum formation energies and maximum binding energies of the 20 different instantiations.

III. RESULTS AND DISCUSSION

A. Spatial distribution of binding energies

Figure 2 displays the spatial distribution of binding energies for He_4V clusters in the $\langle 110 \rangle$ symmetric tilt grain boundary system. Recall that the binding energies correspond to the maximum binding energies for all 20 instantiations. The grain boundaries in this figure are arranged in order of increasing misorientation angle. In Figure 2, each atom represents a site where a He_4V cluster was placed and the binding energy was calculated (i.e., each atom is a different simulation). The minimum periodic length for each grain
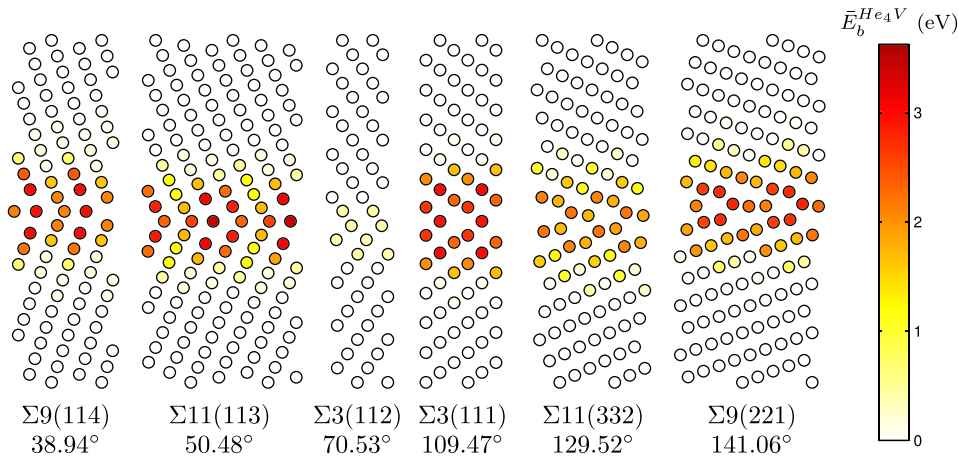
FIG. 2. The binding energies of He_4V clusters in various sites for the six $\langle 110 \rangle$ symmetric tilt grain boundaries. The $\Sigma 3(112)$ grain boundary has much lower binding energies with the He_4V clusters than the other boundaries.

boundary is shown along the horizontal axis and the length from top to bottom is 30 Å, with the grain boundary plane centered in the vertical direction. The binding energy scale shown to the right of Figure 2 ranges from 0 eV (bulk lattice) to the maximum calculated binding energy (3.64 eV for the $\Sigma 13(320)$ GB) from all ten boundaries. The atoms far away from the boundary are white (binding energy of 0 eV), indicating that there is no energy difference over the bulk lattice. As the He_4V cluster gets closer to the grain boundary, there is a GB-affected region with an increased binding energy for the He_nV clusters. The largest binding energies tend to be along the center of the grain boundary plane or along the 1st layer from the GB plane. Furthermore, there is a noticeable symmetry to the binding energies about the grain boundary plane due to the symmetric nature of the grain boundary structure. In terms of variations due to GB structure, the $\Sigma 3(112)$ "twin" grain boundary has a much smaller binding energy in the GB region than all other boundaries in the $\langle 100 \rangle$ and $\langle 110 \rangle$ STGB systems. Interestingly, the $\Sigma 3(112)$ GB has the same disorientation angle, tilt direction, and CSL value as the $\Sigma 3(111)$ GB, but has a very different behavior in terms of the binding behavior with He_nV clusters. Also notice that the $\Sigma 3$ GBs have the lowest and highest GB energies in the present study, which can explain their difference in binding energy behavior. For instance, in a prior study with point defects in Fe,[63] it was found that the formation energies (and consequently, binding energies) for each

particular grain boundary was related to the grain boundary energy. The other nine grain boundaries showed very similar maximum binding energies and binding energy behavior within the grain boundary region, which may be more typical of general high angle grain boundaries. A similar spatial distribution of binding energies is observed for GBs in the $\langle 100 \rangle$ symmetric tilt grain boundary system.

The relative binding energy of the He_nV clusters with respect to the grain boundary structure is also of interest. For instance, Figure 3 shows the spatial distribution of binding energies for four He_nV clusters investigated in the present study for a representative high angle STGB: the $\Sigma 11(113)$ GB. The contour bar for each He_nV cluster is scaled from 0 eV to the maximum binding energy among all 10 GBs for that particular He_nV cluster. Therefore, the represented values are a relative measure with respect to the maximum binding energy for each He_nV cluster to facilitate comparison with respect to the number of He atoms n in the cluster. In many respects, the binding behavior is very similar between the different He_nV clusters. The sites with the largest binding energies appears to stay consistent even as the number of He atoms in a monovacancy increase. However, there are a few subtle differences that are also apparent in Figure 3. First, the interaction length scale of the grain boundary increases as the number of He atoms in the He_nV cluster increases. For instance, there are sites that are several layers away from the GB center with a relatively low relative
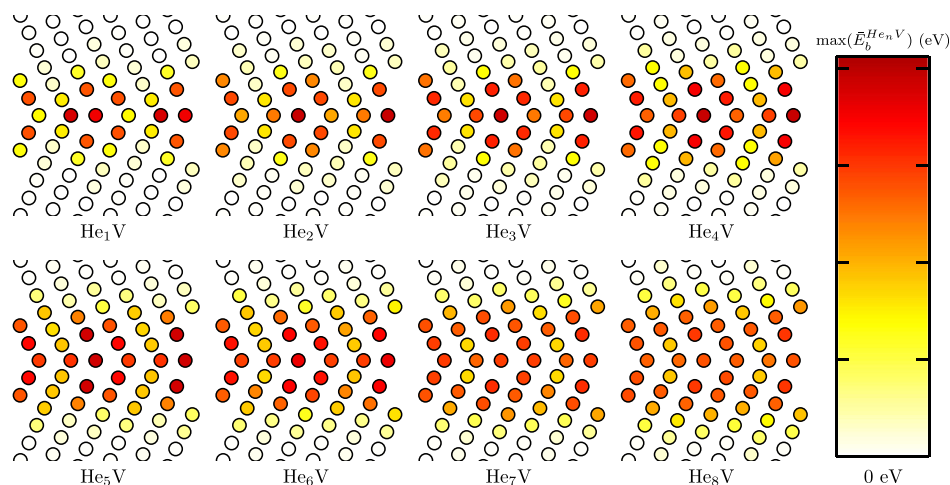

FIG. 3. The binding energies of the eight different He_nV clusters in various sites for a representative high angle grain boundary ($\Sigma 11(113)$ GB). The grain boundary length scale for interaction with He_nV clusters increases with increasing n.

binding energy for He$_1$V, but have a much higher relative binding energy for the He$_8$V cluster. Second, focusing on the atoms within the grain boundary plane, there is less anisotropy in the relative binding energies as the number of He atoms in the He$_n$V cluster increases. Hence, while the grain boundary structure may have a strong influence on the formation and binding energy of He clusters (or even solute atoms and impurities, for that matter) with only a few atoms, this effect may be less pronounced as the size of the cluster binding with the grain boundary increases. In this case, the binding behavior may be more strongly influenced by the reduction in the grain boundary energy.

The behavior in Figure 3 may indicate that the formation and binding energies of lower order clusters may actually be an adequate predictor of the formation energies of higher order clusters. The linear correlation coefficient R is used to compare the degree of correlation between the various formation/binding energies of the He$_n$V clusters, where $R = 1$ indicates a perfect positive correlation and $R = -1$ indicates a perfect negative correlation. In previous work for He defects with ≤ 2 He atoms,[58] the linear correlation coefficient R showed that all the He clusters were correlated with $R > 0.9$, thus suggesting that the local environment strongly influences the He cluster formation energies and that these energies are not independent of one another. Hence, a hypothesis would be that lower order He$_n$V clusters can be used to predict the formation energies of higher order He$_n$V clusters. However, this does not appear to be the case. For instance, Table V lists R values for different combinations of He$_n$V clusters. This table shows that R decreases as the number of He atoms between the two He$_n$V clusters increases. This result is as one might expect. As the size of the He$_n$V cluster increases, the interaction volume of the cluster increases (dilatation) and this results in a lower dependence on the immediate local environment (e.g., shifting behavior from predominantly first nearest neighbors to including second nearest neighbors and beyond). For instance, generally R^2 values above 0.9 are a sign of high correlation; hence the formation (binding) energies of He$_1$V are not good indicators of the formation (binding) energies of He$_8$V ($R = 0.737$), but the formation (binding) energies of He$_7$V are ($R = 0.988$). Last, the positive values indicate positive linear correlation (e.g., as the formation/binding energy for one He$_n$V cluster increases, the formation/binding energy for a second He$_m$V cluster [m $\neq$ n] increases as well); also, it should be noted

that shifting all energies by a scalar and/or multiplying by a scalar, as in the case of formation and binding energies, does not change the value of R.

B. Influence of local GB structure

The local environment surrounding each atom changes as due to interactions with neighboring atoms, which in turn affects the cohesive energy and other per-atom properties. In this subsection, we will analyze several metrics used to characterize the local environment surrounding each atom and compare with the previously calculated formation and binding energies for the different He$_n$V clusters. In this work, six per-atom metrics are examined: the cohesive energy E_{coh}, the hydrostatic stress σ_H, the Voronoi volume V_{Voro}, the centrosymmetry parameter, CS,[80] the common neighbor analysis, CNA,[81–83] and the coordination number, CN. The per-atom virial stress components were used to calculate σ_H utilizing the Voronoi volume consistent with the bulk bcc α-Fe lattice. The per-atom Voronoi volume is also defined from a Voronoi tessellation of the space of the Fe atoms in a clean GB. Previous studies have shown a good correlation between the Voronoi volume and the formation energies of He defects.[56,58] Moreover, DFT studies have shown that increased Voronoi volumes lead to enhanced magnetic moments, higher local energies, and tensile stresses.[73] For CNA and CN, a cutoff distance of 3.5 Å was used and eight nearest neighbors were used to calculate the CSP. Over all GBs, CNA classifies the sites as 85.7% bcc and 14.3% unknown (866 sites total for 10 GBs). The coordination numbers for these sites are 1.2% 11 CN, 2.5% 12 CN, 4.0% 13 CN, 91.0% 14 CN (perfect bcc lattice), 0.6% 15 CN, and 0.7% CN. Hence, there are more undercoordinated sites than overcoordinated sites, as would be expected at the grain boundary (i.e., positive free volume). Furthermore, the per-atom vacancy binding energies E_b^v from Tschopp et al.[62,63] will be compared as part of this analysis, which may be relevant since the He$_n$V clusters involve a monovacancy.

The per-atom metrics were tabulated for all grain boundaries and compared with the He$_n$V clusters to find out which local environmental metrics are correlated. The linear correlation coefficient R is again used to compare the degree of correlation between the local metrics and the binding energies ($R = 1$ indicates a perfect positive correlation and $R = -1$ indicates a perfect negative correlation). The results are shown in Table VI along with results for interstitial He and He$_2$.[58] The binding energies are used instead of formation energies; realize that to change the correlation coefficient R from binding energies E_b to formation energies E_f, a factor of -1 can be applied to all R values in Table VI. The CNA, CSP, and E_{coh} have the highest positive correlation with the binding energies of the He$_n$V clusters (e.g., $R = 0.85$, $R = 0.77$, and $R = 0.76$ for the He$_1$V cluster, respectively). The hydrostatic stress σ_H and CN have the lowest correlation with the He$_n$V cluster binding energies. All metrics have a positive correlation with the binding energies of the He$_n$V clusters except for the coordination number, where undercoordinated atoms have higher binding energies

TABLE V. Linear correlation coefficients R for the formation and binding energies of various He$_n$V clusters with each other.

Cluster	He$_1$V	He$_2$V	He$_3$V	He$_4$V	He$_5$V	He$_6$V	He$_7$V	He$_8$V
He$_1$V	1.000	0.926	0.891	0.864	0.816	0.784	0.752	0.737
He$_2$V	…	1.000	0.985	0.957	0.917	0.888	0.852	0.832
He$_3$V	…	…	1.000	0.981	0.948	0.921	0.887	0.865
He$_4$V	…	…	…	1.000	0.981	0.962	0.932	0.909
He$_5$V	…	…	…	…	1.000	0.987	0.965	0.945
He$_6$V	…	…	…	…	…	1.000	0.984	0.966
He$_7$V	…	…	…	…	…	…	1.000	0.988
He$_8$V	…	…	…	…	…	…	…	1.000

TABLE VI. Linear correlation coefficients R for the local per-atom metrics, E_b^v, and the He$_n$V binding energies.

Cluster E_b	E_b^v	E_{coh}	σ_H	V_{Voro}	CSP	CNA	CN
$E_b^{He_1V}$	0.67	0.76	0.20	0.63	0.77	0.85	−0.46
$E_b^{He_2V}$	0.54	0.60	0.32	0.68	0.75	0.82	−0.34
$E_b^{He_3V}$	0.51	0.57	0.34	0.67	0.73	0.79	−0.32
$E_b^{He_4V}$	0.52	0.57	0.31	0.62	0.70	0.77	−0.31
$E_b^{He_5V}$	0.49	0.55	0.28	0.57	0.65	0.73	−0.31
$E_b^{He_6V}$	0.49	0.54	0.25	0.53	0.61	0.70	−0.30
$E_b^{He_7V}$	0.50	0.53	0.22	0.49	0.57	0.67	−0.30
$E_b^{He_8V}$	0.50	0.53	0.20	0.47	0.55	0.65	−0.30
E_b^{HeInt} [a]	0.57	0.63	0.28	0.65	0.77	0.82	−0.36
$E_b^{He_2Int}$ [a]	0.56	0.63	0.28	0.63	0.75	0.80	−0.34

[a]Interstitial He and He$_2$ binding energies are taken from Ref. 58.

and vice versa. Several metrics have slightly higher correlations for E_b of He$_1$V as well, indicating that as the degree of correlation decreases as the complexity of the He$_n$V cluster increases. In particular, as the number of He atoms in the He$_n$V cluster increases, there is less of a linear correlation with the per-atom local environmental metrics. This result is as expected. The per-atom metrics refer to the unstrained environment prior to inserting the He$_n$V cluster; with an increasing number of He atoms in a monovacancy, the local environment is under a much larger volumetric strain than in the reference environment.

C. Statistical GB description

The formation energies of the eight He$_n$V clusters can be plotted against the distance from the grain boundary to quantify the evolution of the formation energies (and binding energies) near the GB and to quantify the length scale associated with the He$_n$V clusters. Figure 4 is an example of one such plot for the He$_6$V cluster at various sites at the $\Sigma3(112)$ GB and $\Sigma11(332)$ GB. In this plot, the formation energies $E_f^{He_6V^\alpha}$

of each of the twenty different He$_6$V instantiations were first calculated for each site α and the minimum formation energy $\bar{E}_f^{He_6V^\alpha}$ was subsequently calculated from these values. Next, a grain boundary region was defined to compare the different He$_n$V clusters and the different GBs examined in the current work. This grain boundary region was subsequently used to quantify three parameters: the segregation length scale l_{GB}, the mean binding energy $\tilde{E}_b^{mean}$, and the maximum binding energy $\tilde{E}_b^{max}$. The length scale parameter l_{GB} is calculated by first defining a subset β of all sites α based on deviation of formation energies from the bulk formation energy, i.e.,

$$\beta = \left\{ \alpha | \bar{E}_f^{He_nV^\alpha} \leq 0.99 E_f^{bulk} \right\}, \tag{5}$$

and then calculating the bounds of the grain boundary affected region, i.e.,

$$\begin{aligned} x_{min} &= \min(\mathbf{x}^\beta), \\ x_{max} &= \max(\mathbf{x}^\beta), \\ l_{GB} &= x_{max} - x_{min}, \end{aligned} \tag{6}$$

where β is a subset of all sites α where the above condition is met and $\mathbf{x}^\beta$ is the vector containing the coordinates of all sites β in the direction perpendicular to the grain boundary plane. In the subsequent plots and analysis, the coordinate for the grain boundary plane was shifted such that $x = 0$ is the center of the grain boundary and there is an equal distance to the bounds of the grain boundary affected region, x_{min} and x_{max}. Then, to calculate the average binding properties of the grain boundary affected region, a subset γ that contains all sites within the grain boundary affected region is defined, i.e.,

$$\gamma = \left\{ \alpha | x_{min} \geq \mathbf{x}^\alpha \geq x_{max} \right\}. \tag{7}$$

Note that γ and β are not necessarily equivalent sets since γ includes all sites within the grain boundary region and β
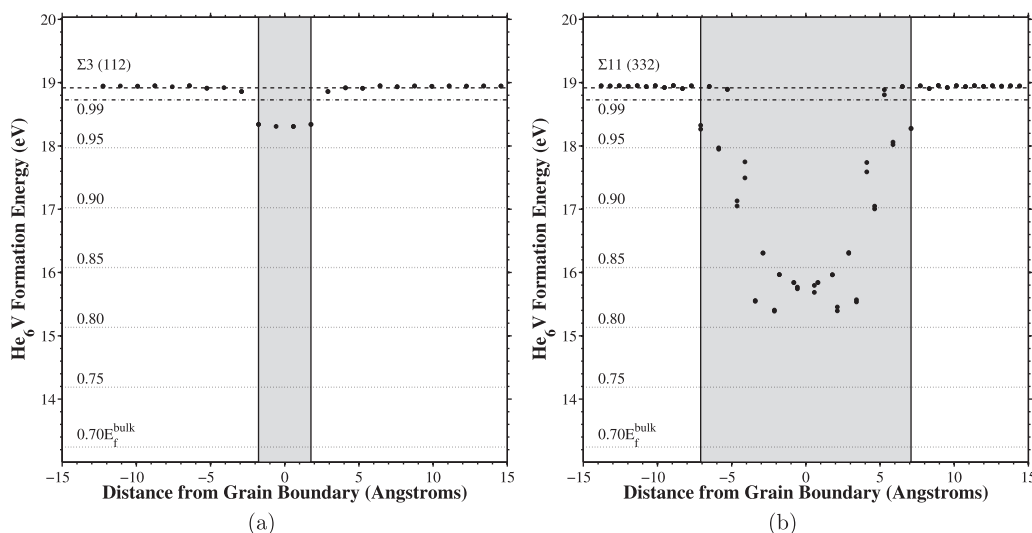

FIG. 4. The formation energies of He$_6$V cluster in various sites plotted against the distance from the grain boundary for the (a) $\Sigma3(112)$ and (b) $\Sigma11(332)$ GBs, which indicates both the lower length scale of interaction and the lower binding energy of the $\Sigma3(112)$ grain boundary.

included only those sites with formation energies that were different from the bulk ($\leq 0.99 E_f^{bulk}$). The mean and maximum binding energies to the grain boundary from the bcc Fe single crystal lattice for a particular He_nV cluster are now given by

$$\tilde{E}_b^{mean} = \frac{1}{n_\gamma} \sum_{\gamma=1}^{n_\gamma} \bar{E}_b^{He_nV^\gamma} \qquad (8)$$

and

$$\tilde{E}_b^{max} = \max\left(\bar{E}_b^{He_nV^\gamma} \right), \qquad (9)$$

where the summation sign in Eq. (8) operates over the number of γ sites n_γ within the specified length scale l_{GB}. Hence, the following steps were also utilized to remove any bias due to simulation cell size or differences between different grain boundaries. First, the difference between the He_nV formation energies at distances >10 Å from the boundary and the He_nV formation energy calculated in a 2000 atom single crystal unit cell (Table IV) was calculated for each boundary to remove any bias. Prior simulations testing for convergence of formation energies as a function of simulation cell size show that this bias was associated with the simulation cell size. The simulation cell sizes given in Table I produced a bias on the order of $0.01 E_f^{bulk}$ or less. The GB-affected region (Eq. (6)) is shaded light gray in Fig. 4 and is bounded by the coordinates x_{min} and x_{max}, which corresponds to sites where the formation energies first deviate by more than $0.01 E_f^{bulk}$ from the bulk formation energy E_f^{bulk} ($0.99 E_f^{bulk}$ is one of the dashed lines in Figure 4). The minimum length that encompasses all these GB sites is l_{GB}. Next, the formation energies were converted to binding energies for each He_nV cluster/GB combination to compare the energy gained by each defect segregating to the boundary as opposed to the bulk lattice. Both the mean and maximum binding energies ($\tilde{E}_b^{mean}$ and $\tilde{E}_b^{max}$ in Eqs. (8) and (9), respectively) for this region are then calculated. To illustrate the percent difference from the bulk formation energy, increments of $0.05 E_f^{bulk}$, or 5% of the bulk formation energy, are indicated by dotted lines in Figure 4. For instance, in the $\Sigma 11(332)$ GB, the maximum binding energy is ≈20% of the bulk formation energy (i.e., ≈$0.80 E_f^{bulk}$) and lies towards the center of the grain boundary region. This technique for identifying three parameters for He segregation was subsequently applied to all 10 GBs for all He_nV clusters.

The length scale l_{GB}, mean binding energy $\tilde{E}_b^{mean}$, and maximum binding energy $\tilde{E}_b^{max}$ for all eight He_nV clusters to the ten grain boundaries examined in the current study is tabulated in Tables VII–IX, respectively. It is immediately apparent that the $\Sigma 3(112)$ twin boundary has a smaller length scale and smaller binding energies than the other boundaries. As observed in Table I, this boundary has both the lowest energy and lowest free volume, which supports that these macroscale GB parameters may indicate lower binding energies with He defects (e.g., as suggested by Kurtz et al.[48]). The other boundaries have very similar length scales (typically between 8 Å to 12 Å) and binding energies (sensitive to He defect type), with a few instances where one boundary has an interaction

TABLE VII. Length scale l_{GB} for various He_nV clusters for the ten grain boundaries (all values are in Å), as calculated using a 1% E_f^{bulk} criterion.

GB Type	He_1V	He_2V	He_3V	He_4V	He_5V	He_6V	He_7V	He_8V
$\Sigma 3(111)$	7.0	8.5	8.5	8.5	13.5	13.5	13.5	16.0
$\Sigma 3(112)$	3.5	3.5	3.5	3.5	3.5	3.5	3.5	5.9
$\Sigma 5(210)$	8.0	10.5	11.2	10.5	12.4	12.4	12.4	14.4
$\Sigma 5(310)$	7.5	5.8	5.8	5.8	7.5	7.5	8.4	9.4
$\Sigma 9(221)$	8.3	10.6	10.6	10.6	11.6	12.6	14.9	15.4
$\Sigma 9(114)$	6.4	9.1	10.4	10.4	11.8	11.8	11.8	13.1
$\Sigma 11(113)$	8.0	10.6	10.6	11.5	11.5	11.5	11.5	14.0
$\Sigma 11(332)$	8.2	9.3	9.3	11.7	11.7	14.2	14.2	16.6
$\Sigma 13(510)$	7.5	8.7	10.3	9.2	10.9	10.9	10.9	10.9
$\Sigma 13(320)$	13.1	17.2	17.2	18.9	18.9	20.0	20.0	21.2

TABLE VIII. Mean binding energy $\tilde{E}_b^{mean}$ to the grain boundary from the bcc Fe single crystal lattice for various He_nV clusters for the ten grain boundaries (all values are in eV), as calculated using a 1% E_f^{bulk} criterion.

GB Type	He_1V	He_2V	He_3V	He_4V	He_5V	He_6V	He_7V	He_8V
$\Sigma 3(111)$	0.41	1.26	2.08	2.52	2.45	3.10	4.05	4.04
$\Sigma 3(112)$	0.07	0.10	0.20	0.28	0.41	0.44	0.47	0.68
$\Sigma 5(210)$	0.37	0.75	1.24	1.69	2.27	2.75	3.64	3.87
$\Sigma 5(310)$	0.33	1.03	1.68	2.28	2.77	3.31	3.69	4.74
$\Sigma 9(221)$	0.35	0.81	1.28	1.75	2.36	2.82	3.03	3.79
$\Sigma 9(114)$	0.45	0.84	1.23	1.67	2.17	2.83	3.66	4.15
$\Sigma 11(113)$	0.31	0.62	1.07	1.50	2.15	2.71	3.59	3.87
$\Sigma 11(332)$	0.29	0.70	1.13	1.27	1.93	2.03	2.58	2.88
$\Sigma 13(510)$	0.35	0.75	1.03	1.67	2.18	2.60	3.38	4.29
$\Sigma 13(320)$	0.19	0.41	0.70	0.86	1.33	1.61	2.08	2.68

TABLE IX. Maximum binding energy $\tilde{E}_b^{max}$ to the grain boundary from the bcc Fe single crystal lattice for various He_nV clusters for the ten grain boundaries (all values are in eV), as calculated using a 1% E_f^{bulk} criterion.

GB Type	He_1V	He_2V	He_3V	He_4V	He_5V	He_6V	He_7V	He_8V
$\Sigma 3(111)$	0.79	1.49	2.65	3.02	4.23	4.89	6.35	7.72
$\Sigma 3(112)$	0.13	0.17	0.31	0.42	0.58	0.64	0.72	0.88
$\Sigma 5(210)$	0.75	1.69	2.44	2.99	4.10	4.94	6.02	6.97
$\Sigma 5(310)$	0.68	1.35	2.27	2.76	3.42	4.01	4.84	6.20
$\Sigma 9(221)$	0.79	1.56	2.41	2.83	4.34	4.91	6.13	7.11
$\Sigma 9(114)$	0.71	1.54	2.37	3.00	4.05	4.60	5.73	6.73
$\Sigma 11(113)$	0.75	1.76	2.71	3.43	4.28	4.89	5.44	6.42
$\Sigma 11(332)$	0.49	1.22	1.92	2.23	3.00	3.56	4.45	5.64
$\Sigma 13(510)$	0.79	1.86	2.91	3.63	4.42	5.17	6.35	7.41
$\Sigma 13(320)$	0.83	1.78	2.63	3.48	4.60	5.61	7.25	8.76

length scale or binding energies different from the rest (e.g., the $\Sigma 13(320)$ GB consistently has the largest GB-affected region). As a general trend, the length scale l_{GB} increases with increasing number of He atoms n for the He_nV cluster types (Table VII). Moreover, both the mean and maximum binding energies (Tables VIII and IX) also increase with increasing n.

D. Atomistically informed model for binding energy distribution

The change in binding energies of He_nV clusters as a function of distance from the GB center can also be analyzed

by binning the energies and calculating the statistics associated with each bin (Figure 5). Due to the symmetric nature of the GB formation and binding energies as a function of distance (e.g., Figure 4), the absolute value of the distance from the GB center was used to provide more data points for the statistical analysis. Furthermore, the energies are split into 1 Å bins to characterize the distributions and compute statistics for sites at a given distance from the GB. For example, the 0 Å bin would contain all binding energies for sites within -0.5 Å to $+0.5$ Å from the GB center and then several statistics are calculated from these binding energy distributions. A boxplot (Figure 5) is used to represent the binding energy distribution in each bin, i.e., the minimum, 25% percentile, median, 75% percentile, and maximum binding energies. In the boxplot, the red line in the box is the median, while the bottom and top edges of the blue boxes represent the 25% and 75% quartiles (as shown to the right of each plot). The whiskers extending from the boxes cover the remainder of the range of energies for each bin, and the ends of the whiskers denote the maximum and minimum values of the binding energies for each bin. The mean value of the binding energies in each bin is also plotted in green. Boxplots can be very useful for visualizing any asymmetry in the distribution of energies.

The box plots in Figure 5 encompass all the binding energy data for all He_nV clusters from the nine representative GBs (excluding the $\Sigma 3(112)$). The mean binding energy is largest for sites close to the GB (0 and 1 Å bins), as shown in Figure 5, and it approaches the normalized bulk value of zero as sites are located farther from the boundary. The mean and median values of the binding energies trend together. Similar to the trends found in Table VII, there is a definite length scale associated with He_nV

clusters binding to the grain boundary that is on the order of 4–6 Å from the GB center. For binding energies within the GB region, the distribution of binding energy is slightly skewed (for a symmetric distribution, the red line lies exactly in the middle of the box) with a large degree of variability, as can be seen from both the difference between the minimum and maximum values as well as the magnitude of the interquartile range (height of the boxes, denoting the binding energies associated with the 25% and 75% percentiles). At distances >7 Å, the binding energy distribution trends towards zero, indicating that the overwhelming majority of atomic sites display a binding energy similar to the bulk value.

A model was formulated to capture the formation energy and binding energy distribution evolution as a function of distance for the different He_nV clusters. As the general behavior is symmetric about zero and approaches zero at large distances, an exponential formulation is used to describe the change in the mean μ and standard deviation σ of the binding energy distribution as a function of distance from the grain boundary x

$$\tilde{E}_b^{\{\mu,\sigma\}}(x) = c_1 \exp\left(-\left(\frac{x}{c_2}\right)^{c_3}\right), \qquad (10)$$

where c_1, c_2, and c_3 are model constants. Notice that $c_3 = 2$ will give a form similar to a normal distribution curve, whereby c_1 modifies the height of the normal distribution and c_2 modifies the width of the normal distribution. The c_3 term modifies the slope of the transition region (i.e., diffuse or sharp transition). This normal distribution is a very simple analogy to the He_nV cluster–grain boundary interaction. The c_1 term describing the height of the normal
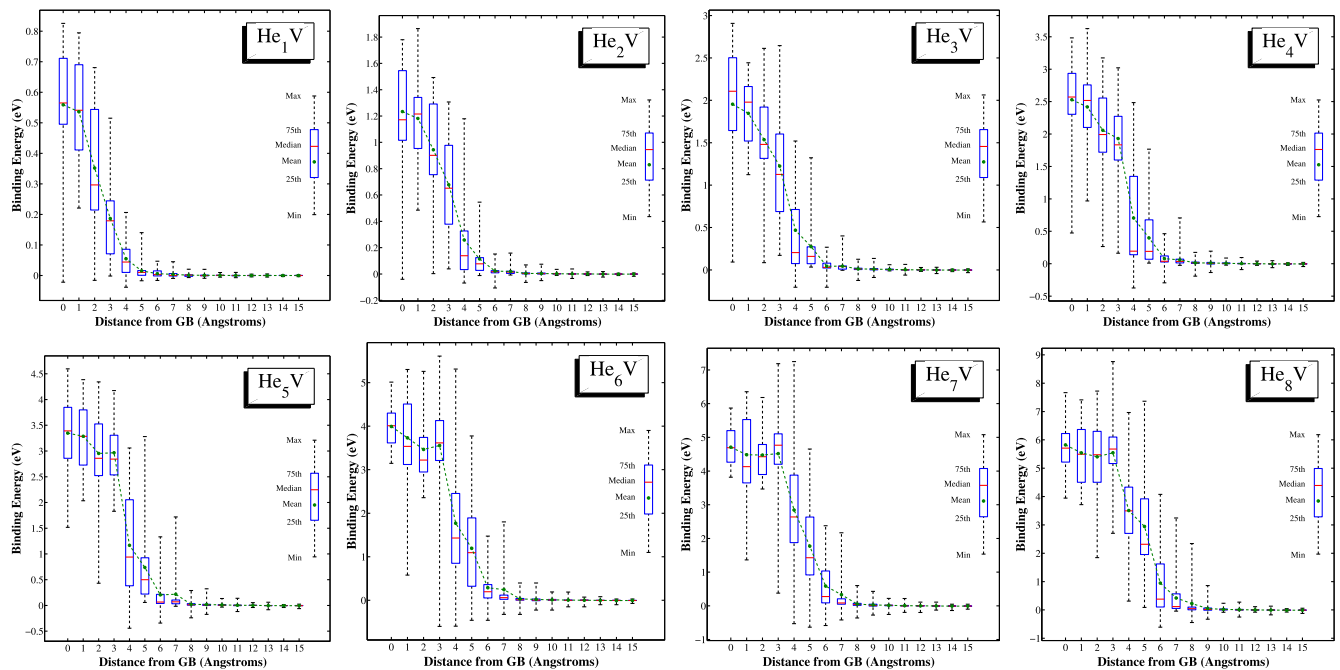

FIG. 5. Boxplots of binding energy as a function of distance from the grain boundary for the nine representative GBs (excluding the $\Sigma 3(112)$) for various He_nV clusters: (top, left to right) He_1V, He_2V, He_3V, He_4V, (bottom, left to right) He_5V, He_6V, He_7V, He_8V. The data is divided into 1 Å bins, and a boxplot is made for each bin. The red lines are medians, the blue box ends are the first and third quartiles, and the black whisker ends are minimum and maximum values. The mean binding energy is also plotted in green.

distribution is related to the maximum binding energy (or minimum formation energy) at the center of the grain boundary. The c_2 term describing the width is related to the length scale. Other model formulations could be used. For instance, a simple linear form could be used. However, even this form would require two constants and it would not capture the actual behavior nearly as well as the present model (based on R^2 analysis). More complicated formulations may better capture this relationship, but at the expense of more constants. For a model with more constants, it may be even less apparent which constants relate to each property. Hence, the present model was chosen as a natural combination of both its simplicity and a direct relationship with the He_nV binding energies and length scales.

Based on an initial nonlinear fit of the data, $c_3 = 2$ was chosen for $\tilde{E}_b^\mu(x)$ and $c_3 = 4$ was chosen for $\tilde{E}_b^\sigma(x)$; these values were kept constant to better assess the change in the constant c_2. Then, a fit of c_1 and c_2 to the mean (in Figure 5) and standard deviation (not shown) curves leads to the values given in Table X for all He_nV clusters. Interestingly, the constant c_1 is related to the mean and maximum binding energy ($\tilde{E}_b^{mean}$ and $\tilde{E}_b^{max}$ in Tables VIII and X, respectively) and the constant c_2 is related to the length scale l_{GB} (Table VII). The root mean square error (RMSE) in Table X increases with an increasing number of He atoms n in the monovacancy and roughly correlates with the constant c_1 (the ratio RMSE/c_1 is shown in parenthesis). The coefficient of determination R^2 for the model given by Eq. (10) tends to decrease with increasing n, but most R^2 values are above 0.90. While additional terms can be added to improve the model agreement, this simple model does show the same trends with c_1 and c_2 as was shown earlier with $\tilde{E}_b^{max}$ and l_{GB}; the length scale increases with increasing n as does the maximum binding energy. Additionally, the present model can be modified to obtain the variation in formation energies for He_nV clusters, i.e., $\tilde{E}_f^\mu(x) = E_f^{bulk} - \tilde{E}_b^\mu(x)$ and $\tilde{E}_f^\sigma(x) = \tilde{E}_b^\sigma(x)$, where $\tilde{E}_f^{\mu;}(x)$ and $\tilde{E}_f^\sigma(x)$ are the mean and standard deviation of the formation energy distribution with distance from the GB. Such analytical models can capture segregation and binding information from atomistic or quantum simulations for inclusion in higher scale simulations.

IV. CONCLUSIONS

The formation/binding energetics and length scales associated with the interaction between He_nV clusters and grain boundaries in bcc α-Fe were explored. Ten different low Σ grain boundaries from the ⟨100⟩ and ⟨110⟩ symmetric tilt grain boundary systems were used (Table I) along with an Fe–He interatomic potential fit to *ab initio* calculations[15] (Table II). In this work, we then calculated formation/binding energies for 1–8 He atoms in a monovacancy (He_1V–He_8V) at all potential grain boundary sites within 15 Å of the boundary (122106 simulations total). To account for the potential variability in He_nV cluster configurations, 20 different random starting positions for the He_n atoms about each monovacancy were simulated (Figure 1). The present results provide detailed information about the interaction energies and length scales of 1–8 He atoms with grain boundaries for the structures examined. The following conclusions can be drawn about this work:

- The local atomic structure and spatial location within the boundary affects the magnitude of the formation/binding energies for all He_nV clusters (Figs. 2 and 3). In general, grain boundary sites have much lower formation energies and higher binding energies than in the bulk, indicating an energetic driving force for He_nV clusters to reside in grain boundary sites, as would be expected based on the insolubility of He atoms in the Fe lattice and their affinity for vacancies and/or free volume within the grain boundary. This GB affected region visibly extends several planes from the GB center. The maximum binding energy (to the GB) for the He_nV clusters increases with an increasing number of He atoms in the monovacancy (Table IX). Furthermore, the Σ3(112) GB has significantly lower binding energies than all other GBs in this study, in agreement with previous results for interstitial He and He_2.[58]

- The relative binding energy behavior was examined with respect to grain boundary structure (e.g., Figure 3). As n increases, the length scale of the GB-affected region increases and there is less variability in the binding energies with GB structure. In fact, while the binding energy behavior between the He_nV clusters is linearly correlated in a positive sense, this correlation decreases as the number of He atoms between two He_nV clusters increases. Metrics for quantifying or classifying the local structure of each atom site were also compared to the formation/binding energies

TABLE X. Parameters for binding energy as a function of distance (Eq. (10)) for all boundaries except the Σ3(112) GB.

He_nV cluster	$\tilde{E}_b^\mu(x)$, $c_3 = 2$				$\tilde{E}_b^\sigma(x)$, $c_3 = 4$			
	c_1 (eV)	c_2 (Å)	RMSE (eV)	R^2	c_1 (eV)	c_2 (Å)	RMSE (eV)	R^2
He_1V	0.58	2.78	0.011 (0.02)	0.997	0.20	4.07	0.010 (0.05)	0.986
He_2V	1.28	3.42	0.036 (0.03)	0.994	0.39	5.21	0.033 (0.09)	0.962
He_3V	2.01	3.65	0.073 (0.04)	0.991	0.61	5.52	0.078 (0.13)	0.921
He_4V	2.64	3.89	0.153 (0.06)	0.977	0.68	6.00	0.076 (0.11)	0.940
He_5V	3.59	4.24	0.254 (0.07)	0.967	0.79	7.28	0.100 (0.13)	0.927
He_6V	4.18	4.51	0.280 (0.07)	0.971	0.94	7.27	0.207 (0.22)	0.807
He_7V	5.09	4.89	0.373 (0.07)	0.967	1.11	7.56	0.256 (0.23)	0.792
He_8V	6.22	5.13	0.449 (0.07)	0.968	1.26	8.29	0.180 (0.14)	0.908

of He clusters. Trends in per-atom metrics with the He_nV cluster energies were tabulated in the form of linear correlation coefficients (Table VII). While CNA, CSP, cohesive energy E_{coh}, vacancy binding energy E_b^v, and Voronoi volume V_{Voro} all positively correlated with He_n cluster binding energies (with R as high as 0.85, respectively), this correlation generally decreased with increasing n and was never highly correlated ($R > 0.90$).

- The change in formation and binding energies as a function of spatial position (Figure 4) was used to identify a GB affected region and to assess a corresponding length scale, mean binding energy, and maximum binding energy for this region (Tables VIII–X). These plots were additionally reduced via symmetry about the GB plane (Figure 5) to show the evolution of the binding energy distribution as a function of distance from the GB plane for the various He_nV clusters. Based on these results, we formulated a model to capture the evolution of the formation and binding energy of He_nV clusters as a function of distance from the GB center, utilizing only constants related to the maximum binding energy and the length scale.

This work significantly enhances our understanding of the energetics involved with how the grain boundary structure interacts with He_nV clusters and how ultimately this affects He (re-)combination and embrittlement near grain boundaries in polycrystalline steels.

[1]H. Ullmaier, "The influence of helium on the bulk properties of fusion-reactor structural-materials," Nucl. Fusion **24**(8), 1039–1083 (1984).

[2]E. E. Bloom, J. T. Busby, C. E. Duty, P. J. Maziasz, T. E. McGreevy, B. E. Nelson, B. A. Pint, P. F. Tortorelli, and S. J. Zinkle, "Critical questions in materials science and engineering for successful development of fusion power," J. Nucl. Mater. **367–370**, 1–10 (2007).

[3]S. J. Zinkle and J. T. Busby, "Structural materials for fission and fusion energy," Mater. Today **12**(11), 12–19 (2009).

[4]T. Yamamoto, G. R. Odette, H. Kishimoto, J. W. Rensman, and P. F. Miao, "On the effects of irradiation and helium on the yield stress changes and hardening and non-hardening embrittlement of similar to 8Cr tempered martensitic steels: Compilation and analysis of existing data," J. Nucl. Mater. **356**(1–3), 27–49 (2006).

[5]H. Trinkaus and B. N. Singh, "Helium accumulation in metals during irradiation—where do we stand?," J. Nucl. Mater. **323**(2–3), 229–242 (2003).

[6]L. K. Mansur and W. A. Coghlan, "Mechanisms of helium interaction with radiation effects in metals and alloys—a review," J. Nucl. Mater. **119**(1), 1–25 (1983).

[7]R. E. Stoller, "The influence of helium on microstructural evolution—implications for dt fusion-reactors," J. Nucl. Mater. **174**(2–3), 289–310 (1990).

[8]R. Vassen, H. Trinkaus, and P. Jung, "Diffusion of helium in magnesium and titanium before and after clustering," J. Nucl. Mater. **183**(1–2), 1–8 (1991).

[9]B. van der Schaaf, D. S. Gelles, S. Jitsukawa, A. Kimura, R. L. Klueh, A. Moslang, and G. R. Odette, "Progress and critical issues of reduced activation ferritic/martensitic steel development," J. Nucl. Mater. **283–287**, 52–59 (2000).

[10]C. C. Fu and F. Willaime, "*Ab initio* study of helium in alpha-Fe: Dissolution, migration, and clustering with vacancies," Phys. Rev. B **72**(6), 064117 (2005).

[11]C. C. Fu and F. Willaime, "Interaction between helium and self-defects in alpha-iron from first principles," J. Nucl. Mater. **367**, 244–250 (2007).

[12]T. Seletskaia, Y. N. Osetsky, R. E. Stoller, and G. M. Stocks, "Calculation of helium defect clustering properties in iron using a multi-scale approach," J. Nucl. Mater. **351**(1–3), 109–118 (2006).

[13]K. Morishita, R. Sugano, and B. D. Wirth, "MD and KMC modeling of the growth and shrinkage mechanisms of helium-vacancy clusters in Fe," J. Nucl. Mater. **323**(2–3), 243–250 (2003).

[14]K. Morishita, R. Sugano, B. D. Wirth, and T. D. de la Rubia, "Thermal stability of helium-vacancy clusters in iron," Nucl. Instrum. Methods Phys. Res., Sect. B **202**, 76–81 (2003).

[15]F. Gao, H. Q. Deng, H. L. Heinisch, and R. J. Kurtz, "A new fe-he interatomic potential based on *ab initio* calculations in alpha-Fe," J. Nucl. Mater. **418**(1–3), 115–120 (2011).

[16]H. L. Heinisch, F. Gao, R. J. Kurtz, and E. A. Le, "Interaction of helium atoms with edge dislocations in alpha-Fe," J. Nucl. Mater. **351**(1–3), 141–148 (2006).

[17]H. L. Heinisch, F. Gao, and R. J. Kurtz, "Atomistic modeling of helium interacting with screw dislocations in alpha-Fe," J. Nucl. Mater. **367**, 311–315 (2007).

[18]D. Terentyev, N. Juslin, K. Nordlund, and N. Sandberg, "Fast three dimensional migration of he clusters in bcc Fe and Fe-Cr alloys," J. Appl. Phys. **105**(10), 103509 (2009).

[19]L. Yang, H. Q. Deng, F. Gao, H. L. Heinisch, R. J. Kurtz, S. Y. Hu, Y. L. Li, and X. T. Zu, "Atomistic studies of nucleation of he clusters and bubbles in bcc iron," Nucl. Instrum. Methods Phys. Res., Sect. B **303**, 68–71 (2013).

[20]L. Yang, X. T. Zu, Z. G. Wang, F. Gao, H. L. Heinisch, R. J. Kurtz, X. Y. Wang, and K. Z. Liu, "Multiple-interactions of displacement cascades with He-vacancy clusters in alpha-iron: Computer simulations," J. Nucl. Mater. **374**(3), 437–444 (2008).

[21]L. Yang, X. T. Zu, Z. G. Wang, H. T. Yang, F. Gao, H. L. Heinisch, and R. J. Kurtz, "Effects of interatomic potential on He bubble creation by cascades in alpha-iron," J. Appl. Phys. **103**(6), 063528 (2008).

[22]L. Yang, X. T. Zu, H. Y. Xiao, F. Gao, H. L. Heinisch, and R. J. Kurtz, "Defect production and formation of helium-vacancy clusters due to cascades in alpha-iron," Phys. B: Condens. Matter **391**(1), 179–185 (2007).

[23]X. T. Zu, L. Yang, F. Gao, S. M. Peng, H. L. Heinisch, X. G. Long, and R. J. Kurtz, "Properties of helium defects in bcc and fcc metals investigated with density functional theory," Phys. Rev. B **80**(5), 054104 (2009).

[24]L. Ventelon, B. Wirth, and C. Domain, "Helium-self-interstitial atom interaction in alpha-iron," J. Nucl. Mater. **351**(1–3), 119–132 (2006).

[25]D. M. Stewart, Y. N. Osetsky, R. E. Stoller, S. I. Golubov, T. Seletskaia, and P. J. Kamenski, "Atomistic studies of helium defect properties in bcc iron: Comparison of He-Fe potentials," Philos. Mag. **90**(7–8), 935–944 (2010).

[26]D. Stewart, Y. Osetskiy, and R. Stoller, "Atomistic studies of formation and diffusion of helium clusters and bubbles in bcc iron," J. Nucl. Mater. **417**(1–3), 1110–1114 (2011).

[27]E. Hayward and C. Deo, "Synergistic effects in hydrogen-helium bubbles," J. Phys.: Condens. Matter **24**(26), 265402 (2012).

[28]N. Juslin and K. Nordlund, "Molecular dynamics simulations of collision cascades in FeCrHe," Nucl. Instrum. Methods Phys. Res., Sect. B **267**(20), 3420–3423 (2009).

[29]N. Juslin and K. Nordlund, "Pair potential for Fe-He," J. Nucl. Mater. **382**(2–3), 143–146 (2008).

[30]T. Seletskaia, Y. N. Osetskiy, R. E. Stoller, and G. M. Stocks, "Development of a Fe-He interatomic potential based on electronic structure calculations," J. Nucl. Mater. **367**, 355–360 (2007).

[31]W. Wilson and R. Johnson, "Rare gases in metals," *Interatomic Potentials and Simulation of Lattice Defects* (Springer, 1972).

[32]C. J. Ortiz, M. J. Caturla, C. C. Fu, and F. Willaime, "He diffusion in irradiated alpha-Fe: An *ab-initio*-based rate theory model," Phys. Rev. B **75**(10), 100102 (2007).

[33]C. J. Ortiz, M. J. Caturla, C. C. Fu, and F. Willaime, "Influence of carbon on the kinetics of He migration and clustering in alpha-Fe from first principles," Phys. Rev. B **80**(13), 134109 (2009).

[34]C. J. Ortiz, M. J. Caturla, C. C. Fu, and F. Willaime, "Impurity effects on He diffusion in alpha-Fe," J. Nucl. Mater. **386–388**, 33–35 (2009).

[35]D. H. Xu and B. D. Wirth, "Modeling spatially dependent kinetics of helium desorption in bcc iron following he ion implantation," J. Nucl. Mater. **403**(1–3), 184–190 (2010).

[36]C. S. Deo, M. A. Okuniewski, S. G. Srivilliputhur, S. A. Maloy, M. I. Baskes, M. R. James, and J. F. Stubbins, "Helium bubble nucleation in bcc iron studied by kinetic Monte Carlo simulations," J. Nucl. Mater. **361**(2–3), 141–148 (2007).

[37]C. S. Deo, M. A. Okuniewski, S. G. Srivilliputhur, S. A. Maloy, M. I. Baskes, M. R. James, and J. F. Stubbins, "The effects of helium on irradiation damage in single crystal iron," J. Nucl. Mater. **367**, 451–456 (2007).

[38]S. Y. Hu, C. H. Henager, H. L. Heinisch, M. Stan, M. I. Baskes, and S. M. Valone, "Phase-field modeling of gas bubbles and thermal conductivity evolution in nuclear fuels," J. Nucl. Mater. **392**(2), 292–300 (2009).

[39]L. Z. Zhang, M. R. Tonks, P. C. Millett, Y. F. Zhang, K. Chockalingam, and B. Biner, "Phase-field modeling of temperature gradient driven pore migration coupling with thermal conduction," Comput. Mater. Sci. **56**, 161–165 (2012).

[40]R. Janisch and C. Elsasser, "Segregated light elements at grain boundaries in niobium and molybdenum," Phys. Rev. B **67**(22), 224101 (2003).

[41]M. Yamaguchi, Y. Nishiyama, and H. Kaburaki, "Decohesion of iron grain boundaries by sulfur or phosphorous segregation: First-principles calculations," Phys. Rev. B **76**(3), 035418 (2007).

[42]A. Kiejna and E. Wachowicz, "Segregation of Cr impurities at bcc iron surfaces: First-principles calculations," Phys. Rev. B **78**(11), 113403 (2008).

[43]R. Janisch and C. Elsasser, "Growth and mechanical properties of a MoC precipitate at a Mo grain boundary: An *ab initio* density functional theory study," Phys. Rev. B **77**(9), 094118 (2008).

[44]T. Ossowski, E. Wachowicz, and A. Kiejna, "Effect of iron additions on intergranular cohesion in chromium," J. Phys.: Condens. Matter **21**(48), 485002 (2009).

[45]E. Wachowicz and A. Kiejna, "Effect of impurities on structural, cohesive and magnetic properties of grain boundaries in alpha-Fe," Modell. Simul. Mater. Sci. Eng. **19**(2), 025001 (2011).

[46]K. N. Solanki, M. A. Tschopp, M. A. Bhatia, and N. R. Rhodes, "Atomistic investigation of the role of grain boundary structure on hydrogen segregation and embrittlement in alpha-Fe," Metall. Mater. Trans. A **44**(3), 1365–1375 (2013).

[47]N. R. Rhodes, M. A. Tschopp, and K. N. Solanki, "Quantifying the energetics and length scales of carbon segregation to alpha-Fe symmetric tilt grain boundaries using atomistic simulations," Modell. Simul. Mater. Sci. Eng. **21**(3), 035009 (2013).

[48]R. J. Kurtz and H. L. Heinisch, "The effects of grain boundary structure on binding of He in Fe," J. Nucl. Mater. **329**, 1199–1203 (2004).

[49]F. Gao, H. Heinisch, and R. J. Kurtz, "Diffusion of he interstitials in grain boundaries in alpha-Fe," J. Nucl. Mater. **351**(1–3), 133–140 (2006).

[50]R. J. Kurtz, H. L. Heinisch, and F. Gao, "Modeling of He-defect interactions in ferritic alloys for fusion," J. Nucl. Mater. **382**(2–3), 134–142 (2008).

[51]F. Gao, H. L. Heinisch, and R. J. Kurtz, "Migration of vacancies, He interstitials and He-vacancy clusters at grain boundaries in alpha-Fe," J. Nucl. Mater. **386–388**, 390–394 (2009).

[52]D. Terentyev and X. He, "Dimensionality of interstitial He migration in ⟨110⟩ tilt grain boundaries in alpha-Fe," Comput. Mater. Sci. **49**(4), 858–864 (2010).

[53]L. Zhang, X. L. Shu, S. O. Jin, Y. Zhang, and G. H. Lu, "First-principles study of He effects in a bcc Fe grain boundary: Site preference, segregation and theoretical tensile strength," J. Phys.: Condens. Matter **22**(37), 375401 (2010).

[54]L. Zhang, Y. Zhang, W. T. Geng, and G. H. Lu, "Towards theoretical connection between tensile strength of a grain boundary and segregated impurity concentration: Helium in iron as an example," Europhys. Lett. **98**(1), 17001 (2012).

[55]D. Terentyev and X. He, "Effect of Cr precipitates and He bubbles on the strength of ⟨110⟩ tilt grain boundaries in bcc Fe: An atomistic study," Comput. Mater. Sci. **50**(3), 925–933 (2011).

[56]L. Zhang, C. C. Fu, and G. H. Lu, "Energetic landscape and diffusion of He in alpha-Fe grain boundaries from first principles," Phys. Rev. B **87**(13), 134104 (2013).

[57]L. Zhang, Y. Zhang, and G. H. Lu, "Structure and stability of He and He-vacancy clusters at a sigma 5(310)/[001] grain boundary in bcc Fe from first-principles," J. Phys.: Condens. Matter **25**(9), 095001 (2013).

[58]M. A. Tschopp, F. Gao, L. Yang, and K. N. Solanki, "Binding energetics of substitutional and interstitial helium and di-helium defects with grain boundary structure in α-Fe," J. Appl. Phys. **115**, 033503 (2014).

[59]M. I. Baskes and V. Vitek, "Trapping of hydrogen and helium at grain-boundaries in nickel—an atomistic study," Metall. Trans. A **16**(9), 1625–1631 (1985).

[60]R. E. Stoller, S. I. Golubov, P. J. Kamenski, T. Seletskaia, and Y. N. Osetsky, "Implementation of a new Fe-He three-body interatomic potential for molecular dynamics simulations," Philos. Mag. **90**(7–8), 923–934 (2010).

[61]T. Seletskaia, Y. Osetsky, R. E. Stoller, and G. M. Stocks, "Magnetic interactions influence the properties of helium defects in iron," Phys. Rev. Lett. **94**(4), 046403 (2005).

[62]M. A. Tschopp, M. F. Horstemeyer, F. Gao, X. Sun, and M. Khaleel, "Energetic driving force for preferential binding of self-interstitial atoms to Fe grain boundaries over vacancies," Scr. Mater. **64**(9), 908–911 (2011).

[63]M. A. Tschopp, K. N. Solanki, F. Gao, X. Sun, M. A. Khaleel, and M. F. Horstemeyer, "Probing grain boundary sink strength at the nanoscale: Energetics and length scales of vacancy and interstitial absorption by grain boundaries in alpha-Fe," Phys. Rev. B **85**(6), 064108 (2012).

[64]H. Beladi and G. S. Rohrer, "The relative grain boundary area and energy distributions in a ferritic steel determined from three-dimensional electron backscatter diffraction maps," Acta Mater. **61**(4), 1404–1412 (2013).

[65]H. Beladi and G. S. Rohrer, "The distribution of grain boundary planes in interstitial free steel," Metall. Mater. Trans. A **44**(1), 115–124 (2013).

[66]M. N. Rittner, J. R. Weertman, and J. A. Eastman, "Structure-property correlations in nanocrystalline Al-Zr alloy composites," Acta Mater. **44**(4), 1271–1286 (1996).

[67]D. E. Spearot, M. A. Tschopp, K. I. Jacob, and D. L. McDowell, "Tensile strength of ⟨100⟩ and ⟨110⟩ tilt bicrystal copper interfaces," Acta Mater. **55**(2), 705–714 (2007).

[68]M. A. Tschopp and D. L. McDowell, "Asymmetric tilt grain boundary structure and energy in copper and aluminium," Philos. Mag. **87**(25), 3871–3892 (2007).

[69]K. Refson, "MOLDY: A portable molecular dynamics simulation program for serial and parallel computers," Comput. Phys. Commun. **126**(3), 310–329 (2000).

[70]G. J. Ackland, K. D'Mellow, S. L. Daraszewicz, D. J. Hepburn, M. Uhrin, and K. Stratford, "The MOLDY short-range molecular dynamics package," Comput. Phys. Commun. **182**(12), 2587–2604 (2011).

[71]F. Gao, D. J. Bacon, P. E. J. Flewitt, and T. A. Lewis, "A molecular dynamics study of temperature effects on defect production by displacement cascades in alpha-iron," J. Nucl. Mater. **249**(1), 77–86 (1997).

[72]X. Li, W. Liu, Y. Xu, C. S. Liu, Q. F. Fang, B. C. Pan, J.-L. Chen, G.-N. Luo, and Z. Wang, "Principal physical parameters characterizing the interactions between irradiation-induced point defects and several tilt symmetric grain boundaries in Fe, Mo and W," J. Nucl. Mater. **444**(1–3), 229–236 (2014).

[73]S. K. Bhattacharya, S. Tanaka, Y. Shiihara, and M. Kohyama, "*Ab initio* study of symmetrical tilt grain boundaries in bcc Fe: Structural units, magnetic moments, interfacial bonding, local energy and local stress," J. Phys.: Condens. Matter **25**(13), 135004 (2013).

[74]Y. Shibuta, S. Takamoto, and T. Suzuki, "Dependence of the grain boundary energy on the alloy composition in the bcc iron-chromium alloy: A molecular dynamics study," Comput. Mater. Sci. **44**(4), 1025–1029 (2009).

[75]D. Wolf, "Structure and energy of general grain-boundaries in bcc metals," J. Appl. Phys. **69**(1), 185–196 (1991).

[76]M. A. Tschopp and D. L. McDowell, "Structures and energies of sigma 3 asymmetric tilt grain boundaries in copper and aluminium," Philos. Mag. **87**(22), 3147–3173 (2007).

[77]G. J. Ackland, M. I. Mendelev, D. J. Srolovitz, S. Han, and A. V. Barashev, "Development of an interatomic potential for phosphorus impurities in alpha-iron," J. Phys.: Condens. Matter **16**(27), S2629–S2642 (2004).

[78]R. A. Aziz, A. R. Janzen, and M. R. Moldover, "*Ab-initio* calculations for helium—a standard for transport property measurements," Phys. Rev. Lett. **74**(9), 1586–1589 (1995).

[79]P. H. Chen, X. C. Lai, K. Z. Liu, X. L. Wang, B. Bai, B. Y. Ao, and Y. Long, "Development of a pair potential for Fe-He by lattice inversion," J. Nucl. Mater. **405**(2), 156–159 (2010).

[80]C. L. Kelchner, S. J. Plimpton, and J. C. Hamilton, "Dislocation nucleation and defect structure during surface indentation," Phys. Rev. B **58**(17), 11085–11088 (1998).

[81]H. Jonsson and H. C. Andersen, "Icosahedral ordering in the Lennard-Jones liquid and glass," Phys. Rev. Lett. **60**(22), 2295–2298 (1988).

[82]J. D. Honeycutt and H. C. Andersen, "Molecular-dynamics study of melting and freezing of small lennard-jones clusters," J. Phys. Chem. **91**(19), 4950–4963 (1987).

[83]H. Tsuzuki, P. S. Branicio, and J. P. Rino, "Structural characterization of deformed crystals by analysis of common atomic neighborhood," Comput. Phys. Commun. **177**(6), 518–523 (2007).